Structural and Multidisciplinary Optimization (2025) 68:148
https://doi.org/10.1007/s00158-025-04054-3

RESEARCH PAPER

Image fragmented learning for data-driven topology design

Yusibo Yang[1] · Kentaro Yaji[1] · Shintaro Yamasaki[2] · Kikuo Fujita[1]

Received: 11 February 2025 / Revised: 1 May 2025 / Accepted: 3 June 2025

Abstract
This paper proposes a data-driven topology design (DDTD) framework, incorporating *image fragmented learning* that leverages the technique of dividing an image into smaller segments for learning each fragment. This framework is designed to tackle the challenges of high-dimensional, multi-objective optimization problems. Original DDTD methods leverage the sensitivity-free nature and high capacity of deep generative models to effectively address strongly nonlinear problems. However, their training effectiveness significantly diminishes as input size exceeds a certain threshold, which poses challenges in maintaining the high degrees of freedom crucial for accurately representing complex structures. To address this limitation, we split a trained conditional generative adversarial network into two interconnected modules: the first performs dimensionality reduction, compressing high-dimensional data into a lower-dimensional representation, which is then fed into a variational autoencoder (VAE) to generate new low-dimensional data. The second module reconstructs the generated low-dimensional data back into the high-dimensional design space. The effectiveness of the proposed approach is demonstrated through two case studies: the optimization of an L-bracket design problem and a turbulent heat transfer design problem, both involving design variables at a scale unattainable by the conventional VAE-based method.

Keywords Data-driven topology design · Topology optimization · Image fragmented learning · Multi-objective optimization

1 Introduction

Topology optimization is a computational design methodology that formulates a structural optimization problem as a material distribution problem within a predefined design domain, offering a high degree of design freedom for achieving an optimal structure (Bendsøe and Kikuchi 1988). By strategically manipulating material layout, this approach facilitates the discovery of innovative solutions that are often unattainable through conventional design methods. Over the past few decades, a diverse range of topology optimization techniques have been developed and successfully applied across various engineering fields, including structure, heat, fluids, and many other engineering problems (Bendsøe and Sigmund 2004; Deaton and Grandhi 2014).

Despite its potential, topology optimization using gradient-based methods often encounters challenges in addressing the multimodal nature of nonlinear physical problems, making it prone to converging on local optima. This limitation has spurred interest in sensitivity-free methods, which circumvent the need for sensitivity analysis and exhibit broader applicability. Genetic algorithms (GAs) (Balamurugan et al. 2008; Wang and Tai 2004), and immune algorithms (Luh and Chueh 2004) have been proposed as effective tools for gradient-free solution search. Similarly, Wu and Tseng (2010) recommended that differential evolution based on a binary bit-string framework can be utilized for numerical optimization problems. However, gradient-free methods face limitations, particularly in structural representation flexibility and computational efficiency. As Sigmund (2011) noted, such constraints restrict their applicability to small-scale problems. While gradient-free methods help avoid some challenges of gradient-based approaches, they remain less effective for large-scale, high-dimensional problems with extensive design freedom.

Responsible editor: Graeme James Kennedy

✉ Kentaro Yaji
yaji@mech.eng.osaka-u.ac.jp

[1] Graduate School of Engineering, The University of Osaka, 2-1 Yamadaoka, Suita, Osaka 565-0871, Japan

[2] Graduate School of Information, Production and Systems, Waseda University, 2-7 Hibikino, Wakamatsu, Kitakyushu, Fukuoka 808-0135, Japan

Published online: 12 August 2025

Recent advancements in artificial intelligence (AI) generative models have gained significant attention in various fields, leading to a surge in their integration into topology optimization (Woldseth et al. 2022). For instance, Oh et al. (2019) proposed a deep learning framework that integrates topology optimization with a generative adversarial network (GAN) (Goodfellow et al. 2014) to generate diverse, high-performance designs from limited data, validated through a 2D wheel design case study. Nie et al. (2021) leveraged stress and strain energy density fields derived from initial material distributions as input features for neural networks, enhancing the accuracy and reliability of generative outputs. Lee et al. (2023) employed super-resolution (SR) image reconstruction methods as a generative approach to enhance the resolution of topology optimization results without increasing mesh refinement, yielding much sharper and higher contrast outcomes compared to conventional methods. Furthermore, Jang et al. (2022) introduced a reinforcement learning-based generative design method that maximizes topology design diversity while significantly reducing computational costs through neural network approximations. Guo et al. (2018) presented an innovative method that employs an augmented variational autoencoder (VAE) (Kingma and Welling 2013) to encode 2D topologies into a low-dimensional latent space, enabling efficient design generation. These studies highlight the growing potential of generative models in addressing challenges associated with high design freedom and improving solution quality beyond the capabilities of conventional topology optimization.

Building on these advancements, data-driven topology design (DDTD) proposed by Yamasaki et al. (2021), demonstrated the capability of deep generative models to efficiently produce diverse material distributions from a small set of latent variables, offering a sensitivity-free approach to strongly nonlinear multi-objective problems. Expanding on DDTD, Yaji et al. (2022) introduced data-driven multifidelity topology design (MFTD) to solve complex topology optimization problems, where Non-dominated Sorting Genetic Algorithm II (NSGA-II) (Deb et al. 2002) is used to select promising solutions in the objective space on Pareto dominance and crowding distance, thereby addressing complex multi-objective optimization. Kato et al. (2025) used data-driven MFTD to minimize maximum stress and volume, starting from gradient-based topology optimization solutions using the p-norm stress measure. Luo et al. (2025) proposed a data-driven multifidelity topology design (MFTD) method for fin design in thermal energy storage, combining high-fidelity phase change modeling with low-fidelity topology optimization. Additionally, to enhance convergence stability in high-design-freedom problems, Kii et al. (2024) proposed a new sampling method in the latent space called latent crossover.

Despite advances in DDTD, significant challenges remain in applying deep generative models to high-dimensional problems, particularly in preserving the design freedom required for capturing complex structures. Previous DDTD methods often compress the design space into limited latent representations for efficiency, which can restrict the diversity of generated solutions. This limitation makes it particularly challenging to apply DDTD to high-dimensional problems, such as high-resolution or three-dimensional designs. Yang et al. (2025) attempted to address this using principal component analysis (PCA) to compress data into lower dimensions, serving as input to a VAE. Material distribution was then reconstructed and enriched with new features using PCA. Although PCA can fully reconstruct a dataset with a sufficient number of components, using fewer components may limit design freedom and risk losing important information. This is because PCA selects components based only on variance, potentially omitting critical features essential for meeting design objectives.

In response, our proposed method, *image fragmented learning*, integrates an image transformation neural network (Isola et al. 2017) with original DDTD. By converting design variables into pixel distributions and processing them through image transformation techniques, the framework achieves efficient dimensional compression and reconstruction. By learning smaller structural fragments and leveraging neural network tiling, our method facilitates the efficient handling of high-dimensional problems while preserving fine structural details.

The main contribution lies in enhancing the original DDTD framework through dimensional transformation, which allows the VAE to handle higher-resolution data by compressing input size before training and recovering it after generation. Combined with fragment-based learning and image transformation, the method enables more diverse and detailed solutions in high-dimensional topology optimization. We demonstrate its effectiveness through applications in minimizing maximum stress for an L-bracket design problem and optimizing a turbulent heat transfer problem, showcasing its capability to address complex, high-dimensional design challenges in topology optimization.

The remainder of this paper is structured as follows. Section 2 provides a brief overview of the fundamental concepts and limitations of previous DDTD methods. Section 3 outlines the proposed approach and the associated training framework. Section 4 details the implementation process, followed by the two computational case studies along with their respective results in Sect. 5. Finally, concluding remarks are offered in Sect. 6.

2 Overview of data-driven topology design

2.1 Main concept

Data-driven computing can effectively generate new data based on the patterns contained in a given dataset. This approach has demonstrated good convergence and robustness, particularly in solving nonlinear and linear elasticity problems (Kirchdoerfer and Ortiz 2016; Conti et al. 2018). Building on this foundation, previous works on DDTD (Yamasaki et al. 2021) extended these principles to optimize material distribution using data-driven techniques. By moving beyond conventional sensitivity-based approaches, DDTD aims to leverage known high-performance material distributions in a multi-objective space to generate even better-performing designs.

DDTD iteratively selects high-performance material distributions, referred to as elite data, during each iteration. The elite data are used to train a deep generative model, and as a result, a latent space is constructed. The elite data are distributed according to the learned probability distribution, and new material distributions are generated by sampling this latent space. The generated data are then evaluated in the multi-objective function space, with higher-performing data accepted as new elite data. Through this iterative process, the elite data are continuously updated, leading to improved performance.

The quality of the initial elite data is critical to the success of DDTD. Referring to Yaji et al. (2020) these initial data can be prepared by solving a simpler topology optimization problem, termed low-fidelity optimization, which is computationally efficient and correlated with the target problem. The complex target problem is then evaluated using multi-objective criteria in a process referred to as high-fidelity evaluation.

Central to the original framework of DDTD is a generative model, VAE, which maps the training data into a latent space. In this latent space, new material distributions are generated by sampling from a learned probability distribution. These generated distributions, inheriting key features from the original data, are iteratively refined. By continuously updating the training dataset with higher-performing designs, the method progressively enhances material configurations in a data-driven manner.

2.2 Variational autoencoder

Figure 1 shows the architecture of the VAE, which is the key component to generate new candidates. For a sample dataset $\mathbf{X}^{(1)}, \mathbf{X}^{(2)}, \ldots, \mathbf{X}^{(N)}$, where $\mathbf{X}^{(i)} \in \mathbb{R}^N$, the encoder aims to compress the high-dimensional input data $\mathbf{X}^{(i)}$ to low-dimensional latent variables $\mathbf{z} \in \mathbb{R}^{N_{\mathrm{lt}}}$, where generally $N_{\mathrm{lt}} \ll N$. The decoder aims to reconstruct high-dimensional output data $\mathbf{Y}^{(i)} \in \mathbb{R}^N$ from low-dimensional latent variables. Kingma and Welling (2013) described the VAE as a method designed to approximate the probability distribution $P(\mathbf{X})$ using a model $P_{\boldsymbol{\theta}}(\mathbf{X}^{(i)}) = P(\mathbf{X};\boldsymbol{\theta})$. The parameter $\boldsymbol{\theta}$ is optimized through learning in a way that maximizes the likelihood of $P_{\boldsymbol{\theta}}(\mathbf{X})$. For each data point, the log-likelihood $\log P_{\boldsymbol{\theta}}(\mathbf{X}^{(i)})$ is bounded by the variational lower bound, as follows:

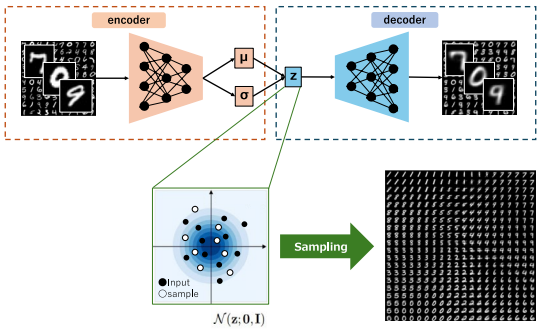

Fig. 1 Schematic illustration of VAE, which is composed of two neural networks, i.e., encoder and decoder

$$\log P_{\boldsymbol{\theta}}(\mathbf{X}^{(i)}) \geq -D_{\mathrm{KL}}(Q_{\boldsymbol{\phi}}(\mathbf{z}|\mathbf{X}^{(i)})||P_{\boldsymbol{\theta}}(\mathbf{z})) + \mathbb{E}_{Q_{\boldsymbol{\phi}}(\mathbf{z}|\mathbf{X}^{(i)})}[\log P_{\boldsymbol{\theta}}(\mathbf{X}^{(i)}|\mathbf{z})]. \tag{1}$$

In this context, $Q_{\boldsymbol{\phi}}(\mathbf{z}|\mathbf{X}^{(i)})$ represents the approximate posterior parameterized by $\boldsymbol{\phi}$, while $D_{\mathrm{KL}}(Q_{\boldsymbol{\phi}}||P_{\boldsymbol{\theta}})$ refers to the Kullback–Leibler (KL) divergence between the distributions $Q_{\boldsymbol{\phi}}$ and $P_{\boldsymbol{\theta}}$. In VAE, because directly maximizing $\log P_{\boldsymbol{\theta}}(\mathbf{X}^{(i)})$ is intractable, $Q_{\boldsymbol{\phi}}(\mathbf{z}|\mathbf{X}^{(i)})$ and $P_{\boldsymbol{\theta}}(\mathbf{X}^{(i)}|\mathbf{z})$, which correspond to the encoder and decoder, are implemented via neural networks. To optimize $\boldsymbol{\theta}$ and $\boldsymbol{\phi}$ using backpropagation, the latent variable $\mathbf{z}$ is defined using the reparameterization trick, as follows:

$$\mathbf{z} = \boldsymbol{\mu} + \boldsymbol{\sigma} \odot \boldsymbol{\epsilon}, \tag{2}$$

where $\boldsymbol{\mu}$ and $\boldsymbol{\sigma}$ represent the mean and the standard deviation of the approximate posterior, respectively. The symbol $\odot$ denotes the element-wise product, and $\boldsymbol{\epsilon}$ is a random sample from the standard Gaussian distribution $\mathcal{N}(\mathbf{0}, \mathbf{I})$. Using (2), it is evident that sampling occurs directly in the latent space, as intended.

Assuming that $Q_{\boldsymbol{\phi}}(\mathbf{z}|\mathbf{X}^{(i)})$, $P_{\boldsymbol{\theta}}(\mathbf{z})$, and $P_{\boldsymbol{\theta}}(\mathbf{X}^{(i)}|\mathbf{z})$ are Gaussian distributions, the VAE loss function L_{VAE} can be expressed as the sum of the analytically derived KL divergence and the mean square error (MSE), from the right-hand side of (1), as follows:

$$\mathcal{L}_{\mathrm{VAE}}(\boldsymbol{\theta},\boldsymbol{\phi};\mathbf{X}^{(i)}) = -\frac{\varrho}{2}\sum_{j=1}^{N_u}(1+\log(\sigma_j^2)-\mu_j^2-\sigma_j^2) + \frac{1}{N}||\mathbf{X}^{(i)}-\mathbf{Y}^{(i)}||^2. \tag{3}$$

Herein, $\varrho \in \mathbb{R}^+$ serves as a weight parameter that modulates the impact of the KL divergence, enforcing the regularization of the latent space toward $\mathcal{N}(\mathbf{0},\mathbf{I})$. The parameters $\boldsymbol{\theta}$ and $\boldsymbol{\phi}$ are optimized using neural networks to minimize L_{VAE}. As a result, the successfully trained model is capable of generating new candidates by sampling from the latent space.

2.3 Limitation on large-scale problem

In density-based structural optimization, increasing the number of mesh elements typically leads to more precise and refined structures, which often exhibit superior performance (Andreassen et al. 2011). Similarly, in DDTD, a higher dimensionality of the design variables expands the potential material distribution possibilities, increasing the likelihood of achieving optimal configurations.

Previously, DDTD has been shown to handle design variables up to 10^4 dimensions (Yamasaki et al. 2021). Within this range, the method is effective due to its use of relatively compact VAE architectures. However, when applied to larger design spaces, this approach faces significant challenges. Scaling up the VAE requires increasing both the number of nodes and layers, which not only raises the computational cost per iteration but also necessitates a higher-dimensional latent space and a larger amount of training data for effective learning. These changes make DDTD evaluations more expensive and less stable.

In practice, once the number of design variables exceeds 10^5, the cumulative runtime for the numerous high-fidelity evaluations in DDTD becomes difficult to manage. Each evaluation becomes significantly more computationally expensive as resolution increases, and the VAE must be trained on increasingly larger datasets to effectively capture the expanded design space. These factors combined lead to unstable training and degraded latent space representations. Moreover, when the number of design variables exceeds 10^5, the original DDTD framework often encounters memory issues under our computing environment (a single NVIDIA RTX A5000 GPU and a single AMD EPYC 7763 CPU). Based on our experience, 10^4 has become a practical upper limit for applying the original DDTD framework under typical computational and data constraints.

Furthermore, even if computational cost is not a constraint, VAE training requires a sufficiently large dataset. When the number of design variables exceeds approximately 10^4, gathering adequate data becomes increasingly difficult, which hinders the learning of meaningful latent features. As noted by Yang et al. (2025), controlling the degrees of freedom for representing material distributions is essential for the effective training of VAEs in DDTD applications. These challenges highlight the inherent difficulties of employing DDTD for large-scale problems.

3 Image fragmented learning

3.1 Basic concept

In this section, we propose a method named image fragmented learning, which integrates dimensionality reduction and enhancement techniques to address the challenges of high computational complexity in topology optimization. This approach segments an image into numerous small square elements, enabling dimensional reduction and upscaling to be applied to each fragment individually.

Specifically, the original high-dimensional data is divided into smaller square elements of size $N_{\mathrm{high}} \times N_{\mathrm{high}}$, as illustrated in Fig. 2. After segmentation, each element is downscaled to $N_{\mathrm{low}} \times N_{\mathrm{low}}$, and a new low-dimensional image is reconstructed by assembling these downscaled segments. The neural network processes these fragments sequentially, enhancing efficiency in handling complex structures.

During the transformation, high-dimensional data is downscaled to generate low-dimensional input for the VAE, which then reconstructs the original high-dimensional data from its output. Instead of generating the entire image at once, the method generates the image block by block using an image-to-image translation neural network, specifically pix2pix (Isola et al. 2017). This block-wise approach simplifies the handling of complex structures while significantly enhancing computational efficiency.

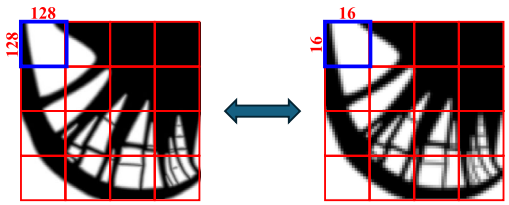

Fig. 2 Fragmentation and reconstruction process for converting between high-dimensional images ($N_{\mathrm{high}} = 128$) and low-dimensional images ($N_{\mathrm{low}} = 16$). The red grid illustrates the segmentation of images, and the blue region highlights the mapping of a representative fragment

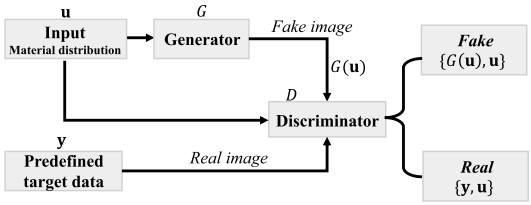

Fig. 3 Process of training pix2pix by cGAN. $\mathbf{u}$: input, $\mathbf{y}$: target, $G(\mathbf{u})$: output by generator G. The discriminator D distinguishes between the real pair $[\mathbf{y}, \mathbf{u}]$ and the fake pair $[G(\mathbf{u}), \mathbf{u}]$

3.2 Division of pix2pix

The concept of dimensionality transformation is inspired by the neural network architecture used in pix2pix, a model designed for image-to-image translation. pix2pix is a variant of the conditional generative adversarial network (cGAN) (Mirza and Osindero 2014), specifically designed to use images as the condition in the generative process, as illustrated in Fig. 3. Unlike standard cGANs, which can use various forms of conditions (e.g., labels or one-hot encoded vectors), pix2pix takes a set of input images $\mathbf{u}^{(1)}, \mathbf{u}^{(2)}, \ldots, \mathbf{u}^{(N)}$, where $\mathbf{u}^{(i)} \in \mathbb{R}^N$, as the conditional input to guide the generation process.

The generator G takes $\mathbf{u}^{(i)}$ along with a noise vector $\boldsymbol{n} \in \mathbb{R}^N$, mapping to the output $\mathbf{y}^{(i)} \in \mathbb{R}^N$, represented as $G : [\mathbf{u}^{(i)}, \boldsymbol{n}] \rightarrow \mathbf{y}^{(i)}$. Here, $\mathbf{y}^{(i)}$ denotes the ground truth used for training, while $G(\mathbf{u}^{(i)})$ represents the actual output image generated by the generator. The training process aims to minimize the discrepancy between $G(\mathbf{u}^{(i)})$ and $\mathbf{y}^{(i)}$.

The role of the discriminator D is trained to accurately distinguish the pair of the real output image $\mathbf{y}^{(i)}$ and the input image $\mathbf{u}^{(i)}$, represented as $[\mathbf{y}^{(i)}, \mathbf{u}^{(i)}]$, as *real*, and the combination of the generated image, $G(\mathbf{u}^{(i)}) \in \mathbb{R}^N$, with the input image, represented as $[G(\mathbf{u}^{(i)}), \mathbf{u}^{(i)}]$, as *fake*. The dynamic interactions between the generator and the discriminator in the pix2pix framework illustrate the adversarial process that drives the network to generate highly realistic images, making both the generator and the discriminator more powerful during training.

For our model, to maintain stable output structures, noise is not introduced as an additional input. The objective of the pix2pix model we used is expressed as:

$$\begin{aligned}\mathcal{L}_{\text{pix2pix}}(G, D) =& \mathbb{E}_{\mathbf{y},\mathbf{u}}[\log D(\mathbf{y}^{(i)}, \mathbf{u}^{(i)})] \\ &+ \mathbb{E}_{\mathbf{y},\mathbf{u}}[\log(1 - D(\mathbf{y}^{(i)}, G(\mathbf{u}^{(i)}))],\end{aligned} \tag{4}$$

where G aims to produce outputs indistinguishable from *real* by the discriminator D, which means G minimizes this objective while D maximizes it, i.e., $G^* = \arg\min_G \max_D \mathcal{L}_{\text{pix2pix}}(G, D)$, $D^* = \arg\max_D \mathcal{L}_{\text{pix2pix}}(G, D)$.

To improve the performance of our model, we combine the GAN objective with a traditional loss function. Specifically, we introduce the L_1 distance as an additional loss term, defined as:

$$\mathcal{L}_{L_1}(G) = \mathbb{E}_{\mathbf{y},\mathbf{u}}[||\mathbf{y}^{(i)} - G(\mathbf{u}^{(i)})||]. \tag{5}$$

By incorporating the L_1 loss, our final objective can be formulated as:

$$G^* = \arg\min_G \max_D \mathcal{L}_{\text{pix2pix}}(G, D) + \lambda \mathcal{L}_{L_1}(G). \tag{6}$$

The generator architecture G uses a U-Net neural network (Ronneberger et al. 2015). As shown in Fig. 4, the encoder employs a series of downsample layers to capture hierarchical feature representations, while the decoder utilizes upsample layers with transposed convolutions to reconstruct the feature maps and match the input resolution. Skip connections between the encoder and decoder enhance predictive performance by directly transferring spatial information across different scales.

As illustrated by the pixel variations across layers in Fig. 4, during the encoder's downsampling process, the width and height of the feature maps are each halved at every layer. Conversely, the decoder restores the feature maps through transposed convolution operations. To leverage the hierarchical structure of the generator G, we decompose the network into two components: a downscale module that maps high-dimensional inputs to lower-dimensional features, and a regeneration module that reconstructs high-dimensional outputs. This process is visually summarized in **PHASE 1** of Fig. 5, and implementation details are further provided in Sect. 4.1.

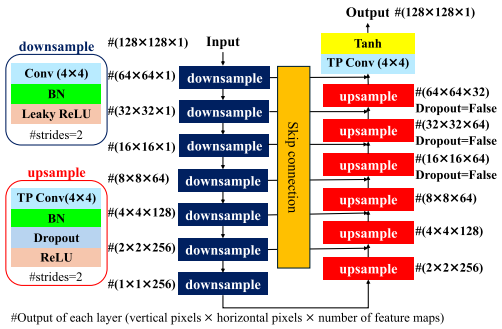

Fig. 4 The U-Net architecture of generator G tailored for processing data with a resolution of 128×128. Each block's output is annotated with its dimensions (vertical pixels × horizontal pixels × feature maps)

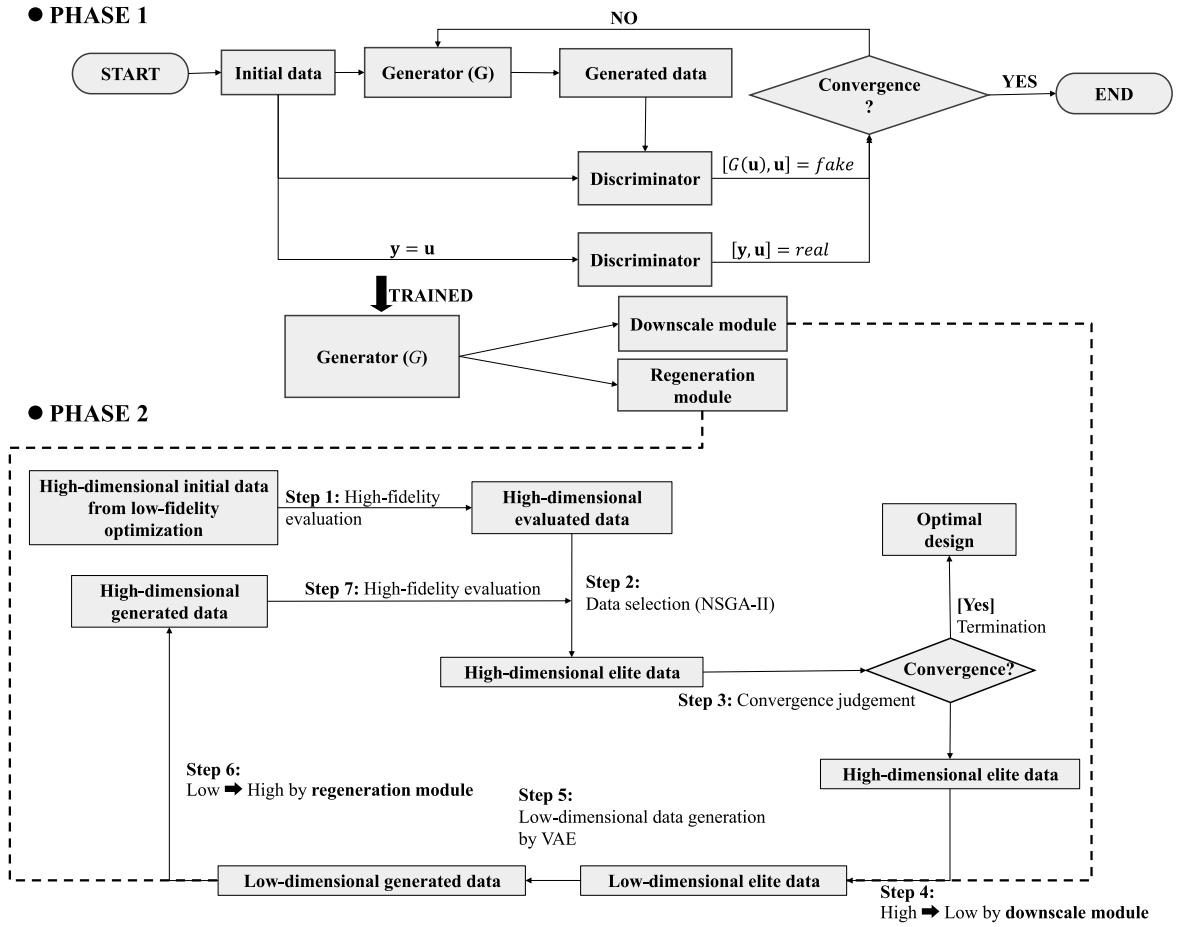

Fig. 5 Flowchart illustrating the data process of proposed image fragmented learning DDTD framework. **PHASE 1** depicts the training of the generative model for dimensionality transformation, while **PHASE 2** demonstrates the iterative optimization process for high-dimensional material distributions

3.3 Overall procedure

Our proposed framework is summarized in Fig. 5. Initially, a small-scale neural network is trained to convert high-dimensional structural fragments into low-dimensional representations. This process develops two essential components: a downscale module for converting high-dimensional fragments ($N_{\text{high}} \times N_{\text{high}}$) to low-dimensional ones ($N_{\text{low}} \times N_{\text{low}}$), and a regeneration module for reconstructing high-dimensional fragments from low-dimensional representations.

After completing the training phase of pix2pix, the framework transitions to the optimization phase for DDTD. This phase incorporates the two modules described in the multifidelity topology design strategy introduced in Sect. 2.1, where low-fidelity optimization refers to applying conventional topology optimization to simplified problems and high-fidelity evaluation denotes the simulation-based assessment of multiple objectives. This entire iterative process is outlined in **PHASE 2** of Fig. 5:

Step 1 Performance Evaluation: Compute the values of multiple objective functions for the high-dimensional initial data.

Step 2 Elite Selection: Identify superior high-dimensional data entities based on their objective values. These selected data are stored for later merging with newly generated high-dimensional data (see **Step 7**). Elitism-based selection is performed using NSGA-II (Deb et al. 2002).

Step 3 Convergence Check: Determine whether the elite high-dimensional data satisfy the convergence criterion.

Step 4 Dimensional Reduction: Convert the high-dimensional elite data into low-dimensional representations using the downscale module. Each structural fragment is processed as described in Sect. 3.1.

Step 5 VAE Training and Generation: Train the VAE on the low-dimensional material distributions and generate new low-dimensional data.

Step 6 Dimensional Regeneration: Reconstruct the high-dimensional data from the newly generated low-dimensional data using the regeneration module from **PHASE 1**.

Step 7 Data Evaluation and Merging: Evaluate the high-dimensional generated data in the same manner as **Step 1**. Merge these generated data, along with their performance values, with the stored data from **Step 2**, and return to **Step 2** for the next iteration.

Through this iterative procedure, the framework identifies high-performance material distributions for high-dimensional problems, which have been challenging to address using previous DDTD methods. By leveraging a two-stage transformation between high- and low-dimensional representations, our framework facilitates efficient exploration of the design space and overcomes the scalability limitations associated with conventional DDTD.

4 Implementation details

This section provides supplementary processes and implementation details necessary for applying the proposed method described in Sect. 3. Specifically, Sects. 4.1 and 4.2 address key considerations when integrating image fragmented learning into the original DDTD framework, while Sect. 4.3 details the application of body-fitted mesh in high-fidelity evaluation.

4.1 Training of pix2pix

As described in Sect. 3.1, the pix2pix model requires paired input and target images during training. To ensure the generation of high-quality material distributions, the network was trained using a dataset of 1600 optimized material distributions derived from various working conditions and boundary constraints in topology optimization (Yamasaki et al. 2019). Each input image was paired with an identical target, enabling the generator to accurately reproduce the input material distributions. However, prior studies such as that by Wang et al. (2018), observed that pix2pix exhibits instability and produces low-quality results when handling high-resolution inputs of 256×256 pixels. To address this, we selected a training dataset with a resolution of 128×128 ($N_{\text{high}} \times N_{\text{high}}$), as shown in Fig. 6, which strikes a balance between computational efficiency and output quality.

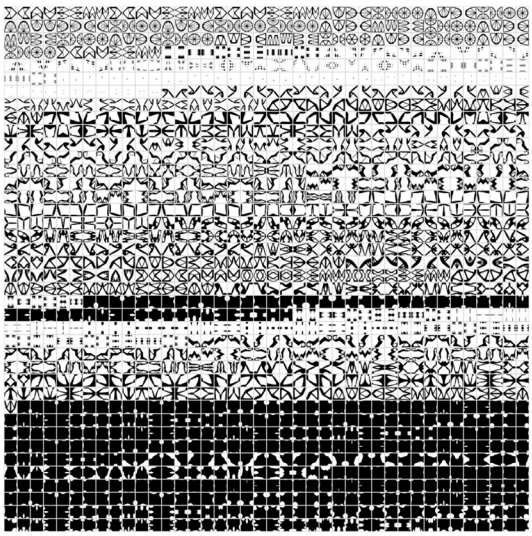

Fig. 6 Training dataset comprising 1600 optimized structures with a resolution of 128×128 pixels from Yamasaki et al. (2019), utilized for training the pix2pix model in this study

The trained pix2pix model is divided into two components: the downscale module, responsible for compressing high-dimensional data into low-dimensional representations, and the regeneration module, which reconstructs low-dimensional data back into the high-dimensional design space. The choice of the downscaled resolution N_{low} is critical because smaller values reduce accuracy, whereas larger values improve reconstruction quality but also increase computational cost and place greater demands on the VAE, as discussed in Sect. 2.

We evaluated the generator model with different values of N_{low} using 40 datasets, each with a resolution of 512×512. The evaluation results indicate that larger N_{low} values yield more accurate image reconstructions. As shown in Fig. 7, the setting of $N_{\text{low}} = 32$ achieves a good balance by significantly reducing resolution while still producing images that closely resemble the original ones, with no noticeable boundaries from segmentation. Although the difference in MSE between $N_{\text{low}} = 16$ and $N_{\text{low}} = 32$ is relatively small, the reconstructed structure at $N_{\text{low}} = 32$ exhibits clearer and sharper contours. Therefore, we selected the generator model with $N_{\text{high}} = 128$ and $N_{\text{low}} = 32$. The architecture of the pix2pix neural network used in our study is illustrated in Fig. 8. After bifurcation, the section highlighted by the dashed line corresponds to the downscale module, while the remaining components form the regeneration module.

The training results after 50 iterations are shown in Fig. 9. The generated outputs closely match the input structures, exhibiting a high degree of structural similarity, indicating that the network successfully learned the mapping between high- and low-dimensional representations. To further

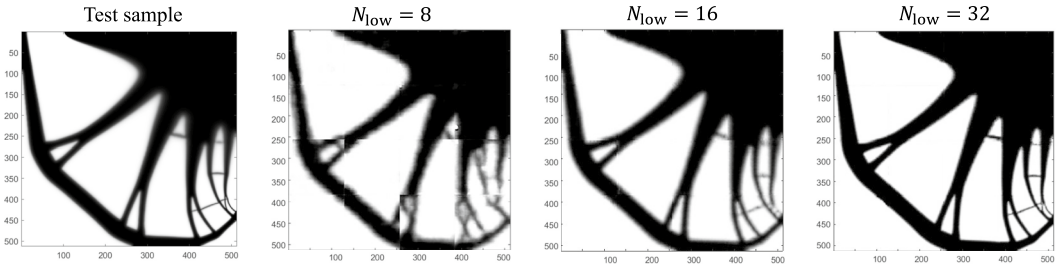

Fig. 7 Reconstruction results of the test sample (size: 512×512) with varying low-dimensional resolutions (N_{low}). The corresponding mean square error (MSE) values are: 0.0701 ($N_{low} = 8$), 0.0079 ($N_{low} = 16$), 0.0074 ($N_{low} = 32$)

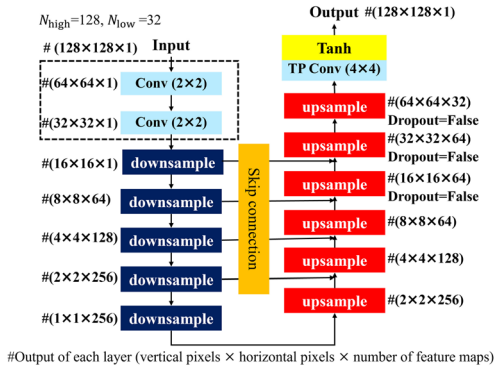

Fig. 8 Architecture of the generator employed in our framework with $N_{high} = 128$, $N_{low} = 32$. Section enclosed by the dashed black box represents the downscale module, and the remaining parts corresponding to the regeneration module

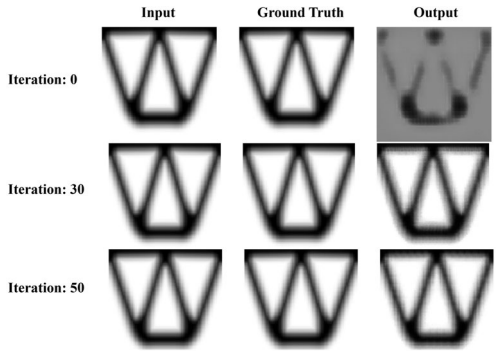

Fig. 9 Training progression of the generator, with input and ground truth set as 128×128

evaluate the generalization capability of the trained model, we tested its performance on an independent set of datasets excluded from the training phase. The results show that the output structures closely match the corresponding inputs, with minimal deviations. This consistency indicates that the model effectively generalizes to unseen data, successfully learning the desired mapping and meeting the design objectives.

4.2 Normalization of material distribution

In the design domain D, material distributions are described using the density expression $\rho(\boldsymbol{\xi})$, where $\boldsymbol{\xi}$ represents the coordinates of an arbitrary point in D. $\rho(\boldsymbol{\xi})$ takes values between 0 and 1, consistent with the density-based approach in topology optimization. In this approach, $\rho = 1$ represents full material presence and $\rho = 0$ represents voids, allowing for intermediate values that facilitate the optimization process.

However, the material distributions generated by the pix2pix-based model are not inherently constrained to the range [0, 1]. Instead, the pix2pix outputs values within the range of $[-1, 1]$.

To align the generated outputs with the density-based framework, we apply a transformation to the material distribution in the design domain D. Specifically, we utilize the scalar function $\phi(\boldsymbol{\xi}) = 2\rho(\boldsymbol{\xi}) - 1$, where $\phi(\boldsymbol{\xi})$ denotes the material distribution representation in both the downscale and regeneration modules of the model. Following dimensional transformation, the material distribution is restored to the desired range using the inverse relation $\hat{\rho}(\boldsymbol{\xi}) = (\phi(\boldsymbol{\xi}) + 1)/2$.

This transformation ensures consistency with the density-based framework, enabling effective structural representation. Using the generated material distribution $\bar{D}$ with $\hat{\rho}(\boldsymbol{\xi})$, the signed distance function $r : \bar{D} \to \mathbb{R}$ is defined as follows:

$$\begin{cases} r(\boldsymbol{\xi}) > 0 \ (\hat{\rho}(\boldsymbol{\xi}) > t_s), \\ r(\boldsymbol{\xi}) = 0 \ (\hat{\rho}(\boldsymbol{\xi}) = t_s), \\ r(\boldsymbol{\xi}) < 0 \ (\hat{\rho}(\boldsymbol{\xi}) < t_s), \end{cases} \tag{7}$$

where t_s is the threshold parameter defined. The smooth transition function H defined as:

$$H(r, h) = \frac{1}{2} + \frac{15}{16}\left(\frac{r}{h}\right) - \frac{5}{8}\left(\frac{r}{h}\right)^3 + \frac{3}{16}\left(\frac{r}{h}\right)^5, \tag{8}$$

where H is differentiable in $[-h, h]$ and $\frac{dH}{dr} = 0$ at $r = -h$ and h, where h is the bandwidth parameter controlling the transition zone from void to material. Following previous DDTD studies (Yamasaki et al. 2021; Yaji et al. 2022), the bandwidth parameter h in the relaxed Heaviside function is set to $3\Delta x$, which balances smoothness and structural resolution. By using a geometry-based reinitialization scheme (Yamasaki et al. 2010), we give $r(\boldsymbol{\xi})$ the signed distance characteristic to the iso-contour of $r(\boldsymbol{\xi}) = 0$. Therefore, the density $\rho(\boldsymbol{\xi})$ is updated using the following relaxed Heaviside function:

$$\hat{\rho}_{\text{data}}(\boldsymbol{\xi}) = \begin{cases} 0 & (r(\boldsymbol{\xi}) < -h), \\ H(r(\boldsymbol{\xi})) & (-h \le r(\boldsymbol{\xi}) \le h), \\ 1 & (h < r(\boldsymbol{\xi})). \end{cases} \tag{9}$$

Through this transformation, the original material distribution is normalized into a smoothed form with a consistent transition zone bandwidth. The application of the Heaviside projection helps reduce noise in the final output, effectively addressing irregularities introduced by the generative model.

4.3 Body-fitted mesh

Figure 10a illustrates an optimized material distribution Ω within the design domain D. In density-based topology optimization, the entire design domain D is typically discretized using regular square meshes. However, the accuracy of the optimized structure is influenced by the mesh shape, potentially introducing numerical artifacts. To address this, the material distribution is extracted and re-discretized using a body-fitted mesh, enabling more precise representation and evaluation of the optimized structure, as depicted in Fig. 10b.

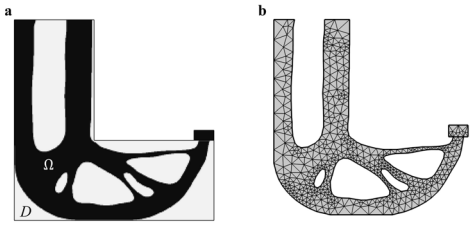

Fig. 10 A sample of discretization with body-fitted mesh of an L-bracket, **a** design domain D and the structure Ω; **b** discretization with body-fitted mesh of Ω

5 Numerical examples

5.1 Example 1: L-bracket design

5.1.1 Problem setting

To verify our framework, we solve a stress minimization and volume minimization problem for a two-dimensional L-bracket, a common benchmark in stress-based topology optimization (Allaire and Jouve 2008; Holmberg et al. 2013). The optimization is challenging due to the nonlinear nature of stress distribution, especially under strict pointwise stress constraints. The maximum von Mises stress often appears on the structural surface, and addressing these peaks is crucial for achieving optimal designs. Additionally, balancing structural efficiency while maintaining low weight and compliance introduces further complexity.

The design domain D and boundary conditions are illustrated in Fig. 11. For the generated material distribution Ω, the bi-objective optimization problem is formulated as:

$$\begin{aligned} &\text{find} && \Omega \subseteq D, \\ &\text{that minimize} && \sigma_{\max} = \max\{\sigma_{\text{vM}}(\boldsymbol{x}) | \forall \boldsymbol{x} \in \Omega\}, \\ & && V = \int_{\Omega} \mathrm{d}\Omega, \end{aligned} \tag{10}$$

where σ_{vM} is the von Mises stress and $\boldsymbol{x}$ represents a point within the material distribution Ω. Due to the non-differentiability of the maximum stress, density-based methods cannot directly solve this original problem. Instead, alternative objective functions are used in the high-fidelity evaluation, leveraging the boundary conditions and material properties given in Table 1.

As noted in Le et al. (2010), maximum stress minimization is hindered by singularities, causing nonlinear

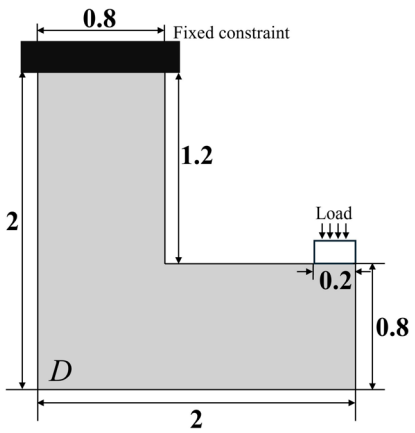

Fig. 11 Design domain and boundary conditions for the L-bracket, D: design domain

algorithms to avoid degenerate regions where global optima often lie, instead converging to local solutions. To address this, the p-norm approximation, denoted as σ_{PN}, is employed in this study to estimate the maximum stress $\sigma_{\max}$ (Kato et al. 2025). Consequently, the low-fidelity optimization problem can be expressed as follows:

$$\begin{aligned} \text{find} \quad & \boldsymbol{\gamma} = (\gamma_1, \gamma_2, \ldots, \gamma_n)^{\mathsf{T}}, \\ \text{that minimize} \quad & \sigma_{\mathrm{PN}} = \left(\sum_{i=1}^{n} \sigma_{\mathrm{vM},i}^{P} \right)^{\frac{1}{P}}, \\ \text{subject to} \quad & V = \sum_{i=1}^{n} v_i \gamma_i \leq \bar{V}, \\ & \gamma_i \in [0, 1], \end{aligned} \tag{11}$$

where v_i is the element, i is the solid volume, and $\bar{V}$ is the volume constraint. According to the previous work (Le et al. 2010), $P = 8$ is set for this study. Table 2 lists the parameters used in the low-fidelity optimization for this case. Under the assumption of linear elasticity and static behavior, the discrete form of the equilibrium equation can be represented as $\mathbf{KU} = \mathbf{F}$, where $\mathbf{K}$ is the stiffness matrix, $\mathbf{U}$ is the displacement vector, and $\mathbf{F}$ is the external force vector. We solve this optimization problem by using the method of moving asymptotes (MMA) (Svanberg 1987), one of the most widely used gradient-based optimizers in the research community of topology optimization.

For compatibility with the image fragmented learning model, the initial design domain is discretized into 262,144 square elements, each acting as a design variable. This level of discretization poses challenges for previous DDTD approaches. We generated an initial dataset comprising 100 material distributions (Fig. 12) via low-fidelity optimization, each with a volume fraction V_f between 0.3 and 0.8. High-fidelity evaluations were performed to assess von Mises stress and structural volume, with iterative refinement aimed at improving design quality.

To efficiently manage the high-dimensional nature of the problem, the mesh is partitioned into 16 equal 128×128 sections (Fig. 13), each compressed to a 32×32 representation. These sections are combined into a latent vector of dimension 16,384 for VAE training, retaining crucial structural details while facilitating efficient processing.

For the VAE training and other DDTD parameters, we adopt the settings as Table 3.

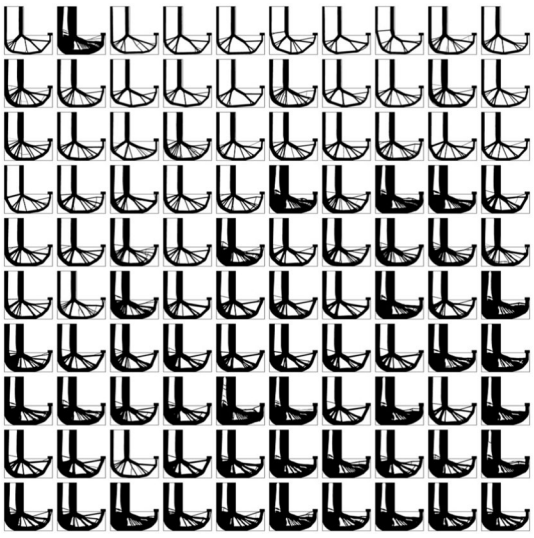

Fig. 12 100 initial structures obtained through topology optimization aimed at minimizing maximum stress

5.1.2 Results and discussion

We evaluate the performance using the hypervolume indicator (Shang et al. 2021) which can measure the convergence performance in multi-objective optimization. For two objectives, it is represented by the area formed between a reference point and the Pareto front in the objective space, as illustrated in Fig. 14. A higher hypervolume indicates improved convergence, implying that the Pareto front has advanced closer to the optimal solution set. Furthermore, a continuously increasing hypervolume throughout the iterations suggests effective optimization progress.

As depicted in Fig. 15a, the hypervolume increases by approximately 68% beyond its initial value after 400 iterations, indicating significant convergence improvement. Moreover, Fig. 15b illustrates the outcome in the objective space for two objectives after 400 iterations, showing improved objective values compared to the initial structure and highlighting superior solutions with smaller volumes

Table 1 Parameters for the high-fidelity evaluation of the L-bracket

Parameter	Value
Young's modulus E	1
Poisson's ratio ν	0.3
Load per area F_{per}	1

Table 2 Parameters for the low-fidelity model of the L-bracket

Parameter	Value
Young's modulus (solid) E_1	1
Young's modulus (void) E_0	1×10^{-9}
Penalty term p	3
Maximum design domain $g_1^{\max}$	2.56
Poisson's ratio ν	0.3
Load per area F_{per}	1

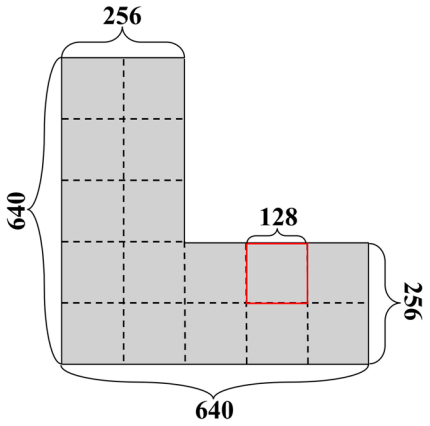

Fig. 13 The L-bracket mesh is segmented into square fragments, each with a size of 128 × 128

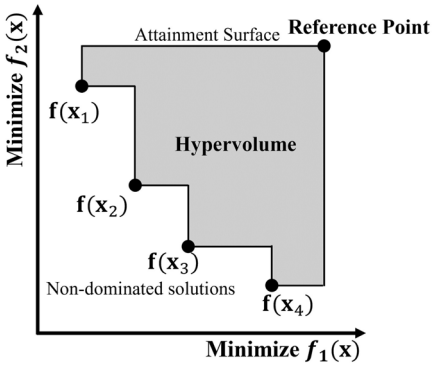

Fig. 14 Illustration of hypervolume in the case of two-objective optimization

and lower maximum stresses. The final structures are clearly clustered into three distinct volume fractions.

We also applied the original DDTD framework to the L-bracket design problem for comparison. Due to the dimensionality limitations imposed by the VAE, the design resolution was set to 16,384. The resulting objective function values after 400 iterations are presented in Fig. 15b. Compared to the original DDTD, the proposed framework based on image fragmented learning enables optimization in significantly higher-dimensional design spaces. As shown in Fig. 15b, the Pareto front obtained by image fragmented learning DDTD clearly dominates that of the original DDTD, demonstrating both lower stress and volume in various regions. This result indicates that the VAE's outputs, once refined through the pix2pix-based regeneration module, better approximate optimized structures under physical simulation. The regenerated high-resolution grayscale images provide more accurate representations of intermediate material states, which leads to improved numerical stability and physical fidelity in high-fidelity evaluations, ultimately resulting in more reliable and effective optimization outcomes.

It should be mentioned that the pix2pix model in this study is trained solely for resolution transformation and does not directly control structural complexity. The pix2pix architecture can be further extended by introducing conditional inputs, which would allow future models to incorporate geometric or performance-related constraints and generate more controllable, topologically diverse high-resolution designs.

Furthermore, the optimized structures obtained by image fragmented learning exhibit notable consistency in local structural features within each volume segment. This consistency is further illustrated in Fig. 16, which shows representative structures on the Pareto front after 400 iterations.

To further evaluate the structural performance, finite element analysis was conducted to examine the stress

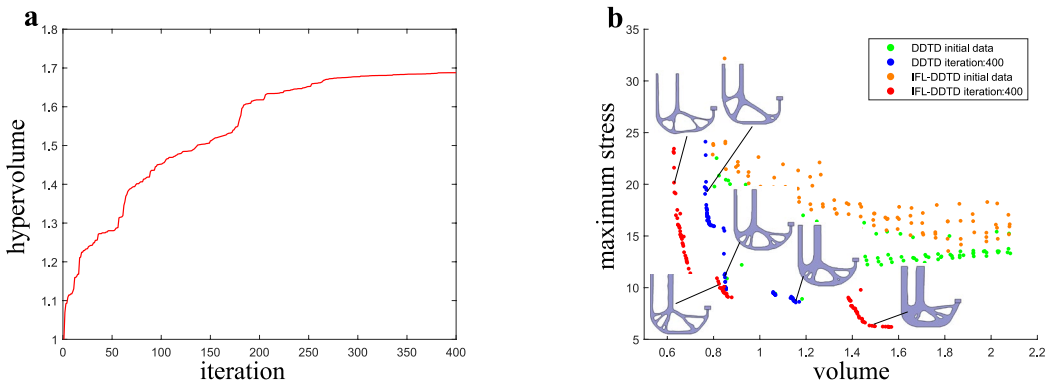

Fig. 15 **a** Hypervolume histories obtained by image fragmented learning DDTD; **b** comparative analysis of objective function values for the proposed method (design dimension: 262,144) and the original DDTD (design dimension: 16,384), along with their respective initial datasets generated by conventional topology optimization. High-fidelity structural images corresponding to both methods are also presented for reference

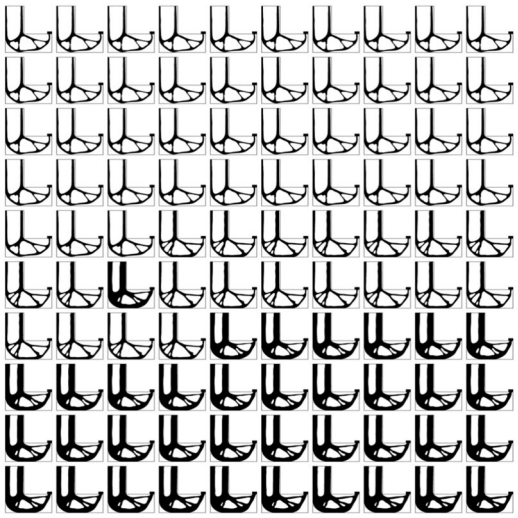

Fig. 16 Obtained material distribution composed of 100 samples of image fragmented learning DDTD on L-brackets design by 400 iterations

distribution in both the initial and optimized structures. Examples of these analyses are presented in Fig. 17, offering insights into the stress behavior across the different designs. The initial structures exhibit sharp corners at the L-joint regions, resulting in significant stress concentrations. These localized stress peaks could lead to structural failure. In contrast, the optimized structures exhibit smoother transitions, effectively reducing stress concentrations and enhancing structural robustness. Moreover, for equivalent material volume fractions, the maximum von Mises stress values in the optimized structures are consistently lower than those in the initial designs. This improvement underscores the enhanced performance of the optimized structures, which are optimized to achieve both stress reduction and efficient material usage. The results highlight the effectiveness of the image-fragmentation learning in producing more robust and reliable designs.

These advantages highlight the potential of image fragmented learning as a significant breakthrough in topology optimization for complex design domain problems, particularly when traditional methods struggle due to dimensionality constraints and performance trade-offs.

5.2 Example 2: turbulent flow heat transfer design

5.2.1 Problem setting

We also applied the proposed framework to the design of a two-dimensional turbulent heat transfer design problem. Additionally, we considered high-dimensional design variables, which were previously infeasible to address using conventional methods.

The design domain is illustrated in Fig. 18. The design variable field is defined as $\gamma = 0$ for solid regions and $\gamma = 1$ for fluid regions. In this turbulent heat transfer problem, the evaluation functionals are governed by the equations for fluid velocity $\mathbf{v}$, pressure p, and temperature T. We employed the

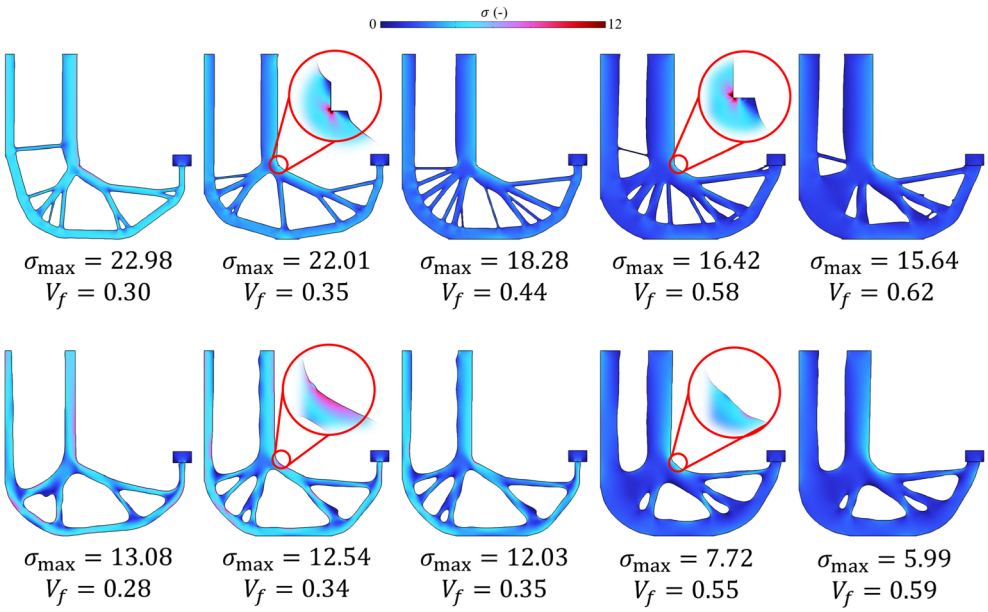

Fig. 17 Comparison of stress distributions between initial structures (top row) and optimized structures (bottom row) in the L-brackets design problem. The maximum von Mises stress ($\sigma_{\max}$) and volume fraction (V_f) are indicated for each case

Table 3 Parameters for the DDTD training process of the L-bracket

Parameter	Value
Input dimension of VAE (N)	16,384
Learning rate of VAE	0.001
Mini-batch size of VAE training	20
Training epochs of VAE	1000
Latent variables of VAE (N_{lt})	8
Weighting coefficient for KL divergence	4
Maximum number of elite data	100
Total number of iterations	400

Reynolds averaged Navier–Stokes (RANS) equation with the standard k-ϵ turbulence model (k is turbulent kinetic energy, ϵ is turbulent dissipation rate) to simulate heat transfer system under the turbulent flow condition:

$$\begin{aligned}
&\nabla \cdot \mathbf{v} = 0,\\
&(\mathbf{v}\cdot\nabla)\mathbf{v} = -\nabla p + \mu\nabla^2\mathbf{v} - \alpha_\gamma \mathbf{v},\\
&(\mathbf{v}\cdot\nabla)k = \nabla\cdot\left[\left(\mu + \frac{\mu_t}{\sigma_k}\right)\nabla k\right] + P_k - \epsilon,\\
&(\mathbf{v}\cdot\nabla)\epsilon = \nabla\cdot\left[\left(\mu + \frac{\mu_t}{\sigma_\epsilon}\right)\nabla \epsilon\right] + C_{\epsilon 1}\frac{\epsilon}{k}P_k - C_{\epsilon 2}\frac{\epsilon^2}{k},\\
&\mathbf{v}\cdot\nabla T = \nabla\cdot\left(\left(\frac{\mu}{Pr} + \frac{\mu_t}{Pr_t}\right)\nabla T\right),
\end{aligned} \tag{12}$$

where μ represents the kinematic viscosity, which is inversely scaled by the Reynolds number Re when the characteristic speed and length are one. The turbulent eddy viscosity μ_t is given by $\mu_t = C_\mu \frac{k^2}{\epsilon}$, where k and ϵ represent the turbulent kinetic energy and its dissipation rate, respectively.

The design-dependent parameter α_γ is defined as 0 in fluid regions and as the inverse permeability α in solid regions. The term P_k represents the production of turbulent kinetic energy caused by velocity gradients and is expressed as:

$$P_k = \mu_t\left[\nabla\mathbf{v} : \left(\nabla\mathbf{v} + (\nabla\mathbf{v})^T\right)\right]. \tag{13}$$

In addition, Pr denotes the Prandtl number, and Pr_t is the turbulent Prandtl number, both critical for thermal transport calculations. The empirical constants used in the turbulence model are as follows: $C_\mu = 0.09$, $C_{\epsilon 1} = 1.44$, $C_{\epsilon 2} = 1.92$, $\sigma_k = 1.0$, and $\sigma_\epsilon = 1.3$.

For this analysis domain in Fig. 18, the boundary conditions applied to Γ_{in} Γ_{out} and Γ_{wall} are defined as follows:

$$\begin{aligned}
\mathbf{v} = -\mathbf{n}, \quad T = 0 \quad &\text{on } \Gamma_{\text{in}},\\
p = 0, \quad \mathbf{n}\cdot\nabla T = 0 \quad &\text{on } \Gamma_{\text{out}},\\
\mathbf{v} = \mathbf{0}, \quad \mathbf{n}\cdot\nabla T = 0 \quad &\text{on } \Gamma_{\text{wall}},\\
T = 1 \quad &\text{on } \Gamma_{\text{heated}},
\end{aligned} \tag{14}$$

Table 4 Parameters for the high-fidelity evaluation of the heat transfer

Parameter	Value
Reynolds number Re	5.0×10^3
Turbulent Prandtl number Pr_t	0.1
Inverse permeability α	1.0×10^4
Maximum design domain $g_1^{\max}$	2

where $\mathbf{n}$ is the outward unit normal vector. The thermal boundary condition $T = 1$ imposed on Γ_{heated} defines the region responsible for heat transfer into the fluid. With the specified boundary conditions, the bi-objective optimization problem for the optimized material distribution of the flow, denoted as Ω, is formulated as follows:

$$\begin{aligned}
&\text{find} \quad \Omega \subseteq D,\\
&\text{that minimize} \quad J_1 = -T_{\text{out}} = -\frac{\int_{\Gamma_{\text{out}}} T \mathrm{d}\Gamma_{\text{out}}}{\Gamma_{\text{out}}},\\
&\qquad\qquad\quad J_2 = p_{\text{in}} = \frac{\int_{\Gamma_{\text{in}}} p \mathrm{d}\Gamma_{\text{in}}}{\Gamma_{\text{in}}},
\end{aligned} \tag{15}$$

where T_{out} represents the average temperature at the outlet, which serves as an indicator of heat transfer efficiency, while p_{in} represents the average pressure at the inlet. These objective functions are applied during the high-fidelity evaluation phase, which is conducted under high Reynolds number conditions to simulate turbulent flow, using the parameters provided in Table 4. A larger T_{out}, corresponding to a smaller J_1, indicates better thermal transfer efficiency of the flow path. Meanwhile, minimizing J_2 reduces pressure losses, thereby enhancing the flow performance.

Given the inherent complexity and nonlinearity of turbulent flow dynamics, we initially used low-fidelity topology optimization based on laminar flow heat transfer as follows:

$$\begin{aligned}
&\nabla\cdot\mathbf{v} = 0,\\
&(\mathbf{v}\cdot\nabla)\mathbf{v} = -\nabla p + \mu\nabla^2\mathbf{v} - \alpha_\gamma\mathbf{v},\\
&\mathbf{v}\cdot\nabla T = \frac{1}{P_e}\nabla^2 T + \beta_\gamma(1-T),
\end{aligned} \tag{16}$$

where Pe is the Péclet number, defined as $Re \cdot Pr$. The Prandtl number Pr corresponds to design variable γ, and the design-dependent parameter α_γ, β_γ are, respectively, given by

$$\begin{aligned}
&Pr = Pr_f + (Pr_s - Pr_f)\frac{1-\gamma}{1+q_k\gamma},\\
&\alpha_\gamma = \alpha^{\max}\frac{1-\gamma}{1+q_f\gamma},\\
&\beta_\gamma = \beta^{\max}(1-\gamma),
\end{aligned} \tag{17}$$

Table 5 Parameters for the low-fidelity model of the heat transfer

Parameter	Value
Reynolds number Re	20, 40, 60, 80
Prandtl number (fluid) Pr_f	10
Prandtl number (solid) Pr_s	1
Control parameter q_k	100
Control parameter q_f	10
Maximum inverse permeability $\alpha^{\max}$	1.0×10^4
Maximum volumetric heat transfer coefficient $\beta^{\max}$	0.1
Maximum design domain $g_1^{\max}$	2

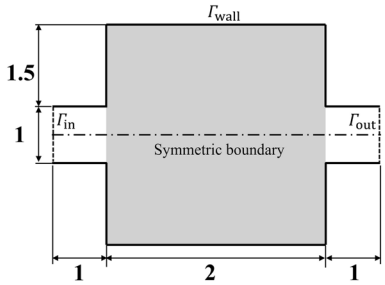

Fig. 18 Design domain and boundary conditions of heat transfer, Γ_{in}: the inlet boundary, Γ_{out}: the outlet boundary, Γ_{wall}: the wall boundary

where q_k and q_f are parameters that control the convexity of Pr and α_γ, respectively. This laminar flow-based low-fidelity model approximates heat transfer characteristics while reducing computational complexity. To maximize heat transfer efficiency, the low-fidelity optimization problem is formulated as follows:

$$\begin{aligned} \text{find} \quad & \boldsymbol{\gamma} = (\gamma_1, \gamma_2, \ldots, \gamma_n)^{\mathsf{T}}, \\ \text{that minimize} \quad & \tilde{J}_1 = -\sum_{i \in \Gamma_{\text{out}}} v_i T_i, \\ \text{subject to} \quad & \gamma_i \in [0, 1], \end{aligned} \tag{18}$$

where v_i and T_i represent the velocity and temperature value of element i, respectively. By employing a low Reynolds number fluid in a laminar flow state, minimizing $\tilde{J}_1$ effectively results in a flow channel that improves heat transfer efficiency and reduce pressure loss. Table 5 summarizes the parameters used in the low-fidelity optimization, which serves as the foundation for subsequent high-fidelity evaluations under turbulent conditions.

To ensure compatibility with the learning framework, the design domain is discretized into a uniform grid consisting of 65,536 square elements. This level of discretization enables the generation of initial designs via low-fidelity topology optimization. However, applying DDTD to such a high-dimensional problem poses significant challenges, particularly in the context of multi-objective turbulence

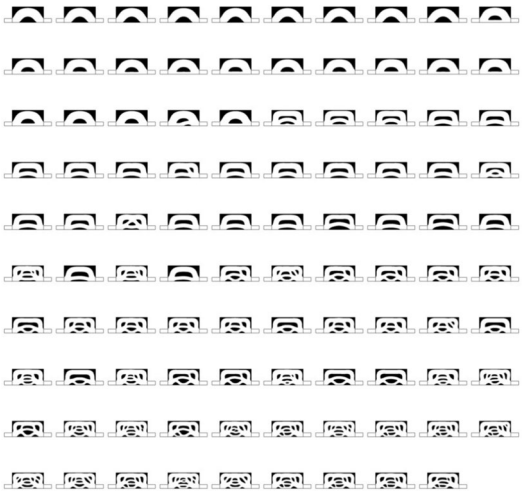

Fig. 19 99 initial data obtained through topology optimization of laminar heat transfer design

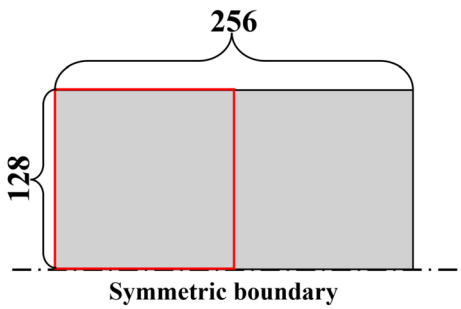

Fig. 20 The symmetric heat transfer mesh is segmented into square fragments, each with a size of 128×128

optimization. Figure 19 presents 99 design samples under varying laminar Reynolds number conditions, as outlined in Table 5.

With the image fragmented learning framework, the design domain is further divided into two equal sections of 128×128 square elements each, as depicted in Fig. 20. Compared to the L-shaped design problem, which involves more intricate handling, this approach proves to be more straightforward and efficient for the structured rectangular design domain. By applying the downscale module, the dimensionality of the input to the VAE is reduced to 2048 design variables, thereby significantly simplifying the problem and rendering it computationally tractable. For the VAE training and other DDTD parameters, we adopt the settings shown in Table 6.

5.2.2 Results and discussion

As in Sect. 5.1.2, the iteration history of the hypervolume indicator in Fig. 21a demonstrates the progression of optimization, showing an improvement of approximately 56% in hypervolume after 400 iterations compared to the initial value. Moreover, Fig. 21b illustrates the enhanced positioning of solutions in the objective space, indicating a marked improvement over the initial dataset. Under identical pressure loss conditions, the optimized structures achieve notably higher thermal transfer efficiency than those in the original dataset.

Similar to the L-bracket case, we also conducted comparative experiments using the original DDTD framework for the heat transfer design problem. Due to dimensional constraints of the VAE, the design resolution was limited to 8192 variables, and the input dimensionality to the VAE was set to 4096. As shown in Fig. 21b, the proposed image fragmented learning DDTD achieves a more favorable Pareto front. This result aligns with the findings from the first case study, further supporting the advantage of high-resolution generation in enhancing simulation-based evaluations.

Figure 22 illustrates 100 representative samples generated by our framework. Compared to the initial dataset, the optimized designs show significantly reduced structural complexity, resulting in designs that are more stable and exhibit distinct shared characteristics. To assess the performance of the generated structures, we conducted simulations to evaluate their thermal and fluid flow behavior. Figure 23 illustrates the simulated temperature, pressure, and velocity fields under comparable flow channel ratios. The results confirm that the optimized structures achieve improved heat

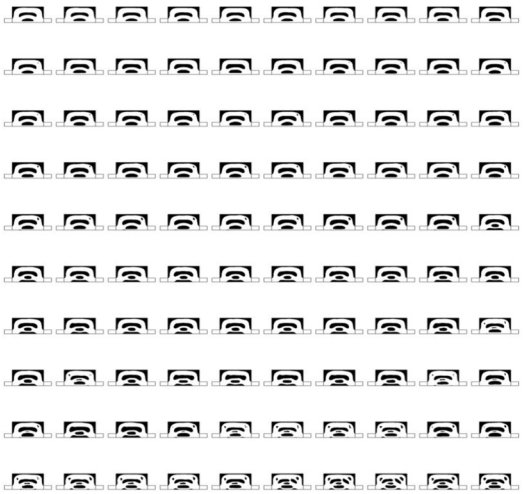

Fig. 22 Obtained dataset composed of 100 samples of image fragmented learning DDTD on two-dimensional turbulent heat transfer by 400 iterations

transfer efficiency while maintaining relatively low pressure losses, demonstrating their effectiveness in optimizing thermal-fluid systems. Figure 24 presents a comparison of heat transfer performance between initial and optimized flow channels under similar pressure drop levels. The optimized channels consistently exhibit enhanced heat transfer efficiency, highlighting the effectiveness of the proposed optimization framework.

6 Conclusion

In this paper, we proposed a framework based on image resolution transformation, called image fragmented learning, which integrates neural network techniques to address

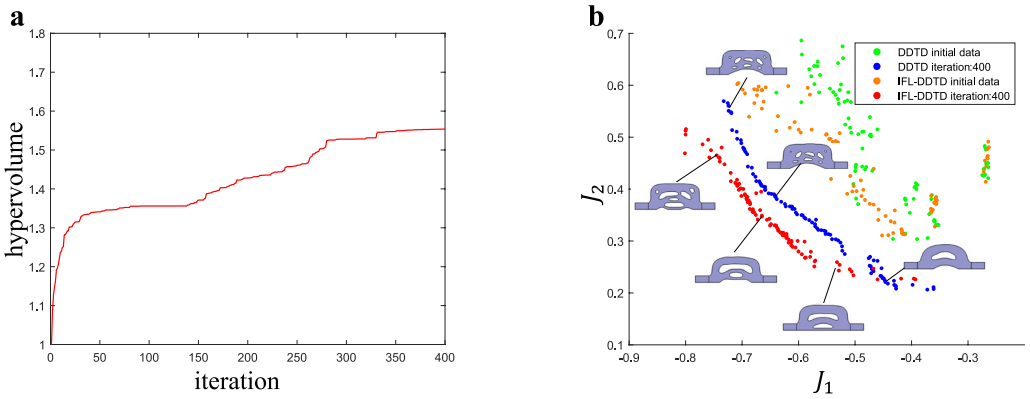

Fig. 21 **a** Hypervolume histories obtained by image fragmented learning DDTD; **b** comparative analysis of objective function values for the proposed method (design dimension: 65,536) and the original DDTD (design dimension: 8192), along with their respective initial datasets generated by conventional topology optimization. High-fidelity structural images corresponding to both methods are also presented for reference

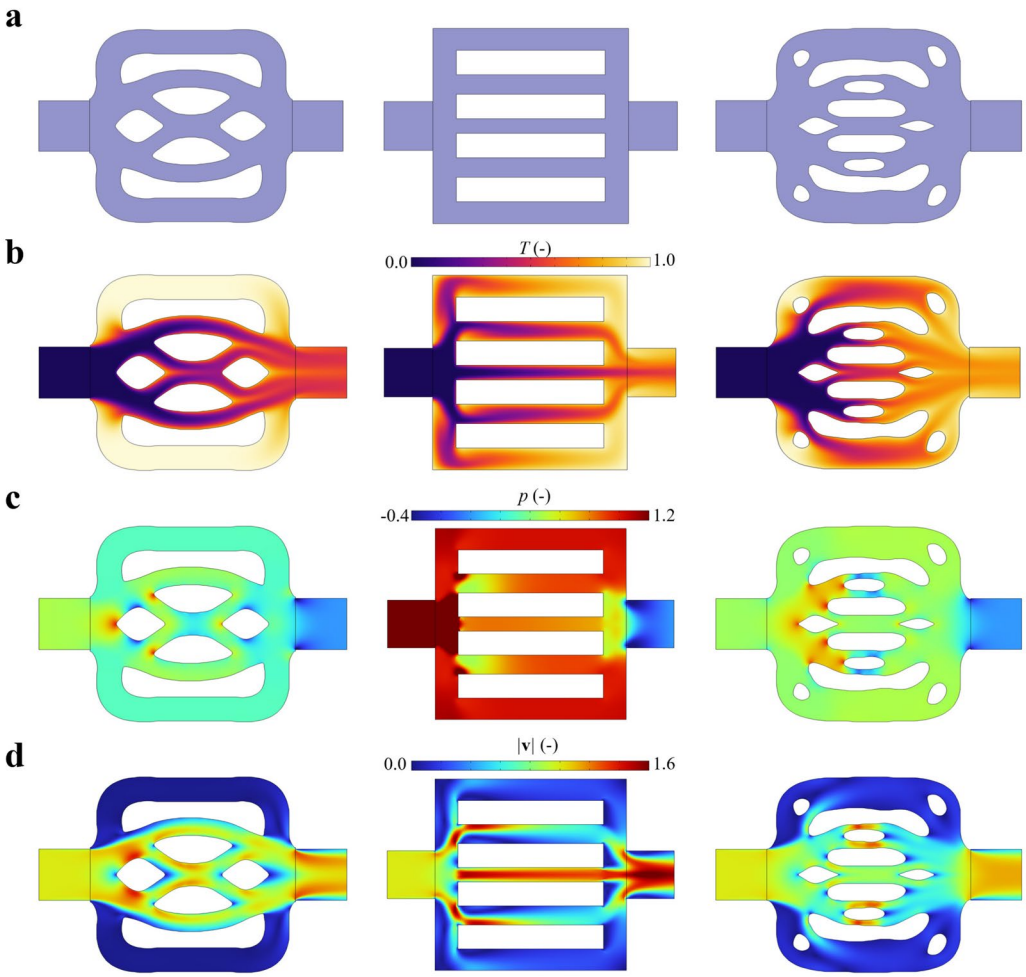

Fig. 23 Comparison of the initial (left), reference straight flow (middle), and optimized (right) configurations in the turbulent heat transfer topology optimization problem: **a** flow channel distribution; **b** temperature; **c** pressure; **d** velocity. All configurations adhere to similar volume constraints, with V_f denoting the ratio of flow channel volume to the design domain. The corresponding values are: $V_f = 0.618, J_1 = -0.544, J_2 = 0.483$ (initial); $V_f = 0.620, J_1 = -0.736, J_2 = 1.504$ (reference); $V_f = 0.623, J_1 = -0.801, J_2 = 0.457$ (optimized)

Table 6 Parameters for the DDTD training process of the heat transfer

Parameter	Value
Input dimension of VAE (N)	2048
Learning rate of VAE	0.001
Mini-batch size of VAE training	20
Training epochs of VAE	1000
Latent variables of VAE (N_{lt})	5
Weighting coefficient for KL divergence	4
Maximum number of elite data	100
Total number of iterations	400

the challenges of high-dimensional, multi-objective optimization in data-driven topology design (DDTD). By utilizing the pix2pix neural network for dimensional transformation and a variational autoencoder (VAE) for data generation, the proposed framework effectively compresses and reconstructs high-dimensional datasets. Consequently, the proposed method enhances the scalability of DDTD to 10^5 design variables, beyond the capabilities of conventional implementations. The effectiveness of this method was demonstrated through two case studies: an L-bracket design and a turbulent heat transfer system.

While the proposed method significantly enhances scalability and optimization performance, its success remains influenced by the quality of initial training data. Moreover, the current solution selection approach, based on

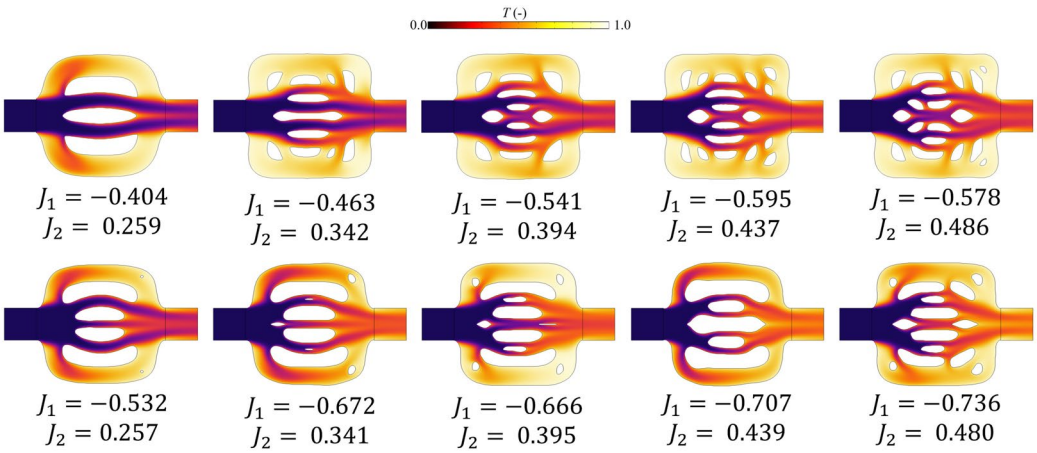

Fig. 24 Comparison of temperature distribution between initial (top row) and optimized (bottom row) flow channels under similar pressure dissipation conditions. The average inlet pressure (J_1) and average outlet temperature (J_2) are indicated for each case

NSGA-II, may benefit from improvements to better capture solution diversity in multi-objective settings. Given its modular and scalable nature, the proposed framework shows strong potential for extension to more complex and three-dimensional design problems. Future work should focus on improving the quality and diversity of the initial low-fidelity designs used for training and exploring applications to higher-dimensional and 3D design domains. The pix2pix network could also be extended beyond resolution mapping to enable more controllable and complex structural generation.

Acknowledgements This work was funded by JSPS KAKENHI (Grant No. 23H03799). And we would like to express our gratitude to Ryutaro Hashimoto for his valuable support on this research.

Author Contributions Yusibo Yang: Writing—original draft, Conceptualization, Methodology, Code editing, Software, Validation, Data curation. Kentaro Yaji: Writing—review & editing, Conceptualization, Methodology, Code editing, Supervision, Resources, Funding acquisition. Shintaro Yamasaki: Writing—review & editing, Methodology, Data preparation. Kikuo Fujita: Writing—review & editing, Conceptualization, Methodology, Supervision, Resources.

Funding Open Access funding provided by The University of Osaka. This work was supported by JSPS KAKENHI Grant Number 23H03799.

Declarations

Conflict of interest The authors declare that they have no Conflict of interest.

Replication of results The manuscript provides sufficient information for the replication of results. Readers interested in further details regarding the implementation or access to numerical codes are encouraged to contact the corresponding author with a reasonable request. The data in this study are also available upon request.

References

Allaire G, Jouve F (2008) Minimum stress optimal design with the level set method. Eng Anal Bound Elem 32(11):909–918. https://doi.org/10.1016/j.enganabound.2007.05.007

Andreassen E, Clausen A, Schevenels M, Lazarov BS, Sigmund O (2011) Efficient topology optimization in MATLAB using 88 lines of code. Struct Multidisc Optim 43(1):1–16. https://doi.org/10.1007/s00158-010-0594-7

Balamurugan R, Ramakrishnan C, Singh N (2008) Performance evaluation of a two stage adaptive genetic algorithm (TSAGA) in structural topology optimization. Appl Soft Comput 8(4):1607–1624. https://doi.org/10.1016/j.asoc.2007.10.022

Bendsøe MP, Kikuchi N (1988) Generating optimal topologies in structural design using a homogenization method. Comput Methods Appl Mech Eng 71(2):197–224

Bendsøe MP, Sigmund O (2004) Topology optimization by distribution of isotropic material. Topology optimization: theory, methods, and applications. Springer, Berlin, pp 1–69

Conti S, Müller S, Ortiz M (2018) Data-driven problems in elasticity. Arch Ration Mech Anal 229(1):79–123. https://doi.org/10.1007/s00205-017-1214-0

Deaton J, Grandhi R (2014) A survey of structural and multidisciplinary continuum topology optimization: post 2000. Struct Multidisc Optim 49(1):1–38. https://doi.org/10.1007/s00158-013-0956-z

Deb K, Pratap A, Agarwal S, Meyarivan T (2002) A fast and elitist multiobjective genetic algorithm: NSGA-II. IEEE Trans Evol Comput 6(2):182–197

Goodfellow I, Pouget-Abadie J, Mirza M, Xu B, Warde-Farley D, Ozair S, Courville A, Bengio Y (2014) Generative adversarial nets. In: Ghahramani Z, Welling M, Cortes C, Lawrence N, Weinberger K (eds) Advances in neural information processing systems, vol 27. Curran Associates Inc, New York, pp 2672–2680

Guo T, Lohan DJ, Cang R, Ren MY, Allison JT (2018) An indirect design representation for topology optimization using variational autoencoder and style transfer. https://doi.org/10.2514/6.2018-0804

Holmberg E, Torstenfelt B, Klarbring A (2013) Stress constrained topology optimization. Struct Multidisc Optim 48(1):33–47. https://doi.org/10.1007/s00158-012-0880-7

Isola P, Zhu JY, Zhou T, Efros AA (2017) Image-to-image translation with conditional adversarial networks. In: Proceedings of the IEEE conference on computer vision and pattern recognition (CVPR). https://doi.org/10.48550/arXiv.1611.07004

Jang S, Yoo S, Kang N (2022) Generative design by reinforcement learning: enhancing the diversity of topology optimization designs. Comput Aided Des 142:103225. https://doi.org/10.1016/j.cad.2022.103225

Kato M, Kii T, Yaji K, Fujita K (2025) Maximum stress minimization via data-driven multifidelity topology design. J Mech Des 147(8):081702. https://doi.org/10.1115/1.4067750

Kii T, Yaji K, Fujita K, Sha Z, Conner Seepersad C (2024) Latent crossover for data-driven multifidelity topology design. J Mech Des 146(5):051713. https://doi.org/10.1115/1.4064979

Kingma DP, Welling M (2013) Auto-encoding variational Bayes. arXiv:1312.6114

Kirchdoerfer T, Ortiz M (2016) Data-driven computational mechanics. Comput Methods Appl Mech Eng 304:81–101. https://doi.org/10.1016/j.cma.2016.02.001

Le C, Norato J, Bruns T, Ha C, Tortorelli D (2010) Stress-based topology optimization for continua. Struct Multidisc Optim 41(4):605–620. https://doi.org/10.1007/s00158-009-0440-y

Lee S, Lieu QX, Vo TP, Kang J, Lee J (2023) Topology optimization using super-resolution image reconstruction methods. Adv Eng Softw 177:103413. https://doi.org/10.1016/j.advengsoft.2023.103413

Luh GC, Chueh CH (2004) Multi-modal topological optimization of structure using immune algorithm. Comput Methods Appl Mech Eng 193(36):4035–4055

Luo JW, Yaji K, Chen L, Tao WQ (2025) Data-driven multi-fidelity topology design of fin structures for latent heat thermal energy storage. Appl Energy 377:124596. https://doi.org/10.1016/j.apenergy.2024.124596

Mirza M, Osindero S (2014) Conditional generative adversarial nets. arXiv:1411.1784

Nie Z, Lin T, Jiang H, Kara L (2021) TopologyGAN: topology optimization using generative adversarial networks based on physical fields over the initial domain. J Mech Des 143(3):031715. https://doi.org/10.1115/1.4049533

Oh S, Jung Y, Kim S, Lee I, Kang N (2019) Deep generative design: Integration of topology optimization and generative models. J Mech Des 141(11):111405. https://doi.org/10.1115/1.4044229

Ronneberger O, Fischer P, Brox T (2015) U-net: Convolutional networks for biomedical image segmentation. In: Navab N, Hornegger J, Wells WM, Frangi AF (eds) Medical image computing and computer-assisted intervention—MICCAI 2015. Springer, Cham, vol 9351, pp 234–241. https://doi.org/10.1007/978-3-319-24574-4_28

Shang K, Ishibuchi H, He L, Pang LM (2021) A survey on the hypervolume indicator in evolutionary multiobjective optimization. IEEE Trans Evol Comput 25(1):1–20. https://doi.org/10.1109/TEVC.2020.3013290

Sigmund O (2011) On the usefulness of non-gradient approaches in topology optimization. Struct Multidisc Optim 43(5):589–596. https://doi.org/10.1007/s00158-011-0638-7

Svanberg K (1987) The method of moving asymptotes—a new method for structural optimization. Int J Numer Methods Eng 24(2):359–373

Wang TC, Liu MY, Zhu JY, Tao A, Kautz J, Catanzaro B (2018) High-resolution image synthesis and semantic manipulation with conditional GANs. In: Proceedings of the IEEE conference on computer vision and pattern recognition (CVPR). https://doi.org/10.48550/arXiv.1711.11585

Wang S, Tai K (2004) Graph representation for structural topology optimization using genetic algorithms. Comput Struct 82(20):1609–1622. https://doi.org/10.1016/j.compstruc.2004.05.005

Woldseth R, Aage N, Bærentzen J, Sigmund O (2022) On the use of artificial neural networks in topology optimisation. Struct Multidisc Optim 65(10):294. https://doi.org/10.1007/s00158-022-03347-1

Wu C, Tseng K (2010) Topology optimization of structures using modified binary differential evolution. Struct Multidisc Optim 42(6):939–953. https://doi.org/10.1007/s00158-010-0523-9

Yaji K, Yamasaki S, Fujita K (2020) Multifidelity design guided by topology optimization. Struct Multidisc Optim 61(3):1071–1085. https://doi.org/10.1007/s00158-019-02406-4

Yaji K, Yamasaki S, Fujita K (2022) Data-driven multifidelity topology design using a deep generative model: application to forced convection heat transfer problems. Comput Methods Appl Mech Eng 388:114284. https://doi.org/10.1016/j.cma.2021.114284

Yamasaki S, Nishiwaki S, Yamada T, Izui K, Yoshimura M (2010) A structural optimization method based on the level set method using a new geometry-based re-initialization scheme. Int J Numer Methods Eng 83(12):1580–1624. https://doi.org/10.1002/nme.2874

Yamasaki S, Yaji K, Fujita K (2019) Knowledge discovery in databases for determining formulation in topology optimization. Struct Multidisc Optim 59(2):595–611. https://doi.org/10.1007/s00158-018-2086-0

Yamasaki S, Yaji K, Fujita K (2021) Data-driven topology design using a deep generative model. Struct Multidisc Optim 64(3):1401–1420. https://doi.org/10.1007/s00158-021-02926-y

Yang J, Yaji K, Yamasaki S (2025) Data-driven topology design based on principal component analysis for 3D structural design problems. Struct Multidisc Optim 68:103. https://doi.org/10.1007/s00158-025-04036-5